Journal of Materials Chemistry A

ROYAL SOCIETY OF CHEMISTRY

PAPER

View Article Online
View Journal | View Issue

Cite this: J. Mater. Chem. A, 2026, 14, 7563

Stable silica-modified zirconia with tunable acidity for enhanced catalytic transfer hydrogenation of levulinic acid and esters to γ-valerolactone

Memoona Khalid,[a] Mark A. Isaacs,[bcd] Stylianos D. Stefanidis,[e] Stamatia S. Karakoulia,[e] Nicole Hondow,[f] Dave Scapens,[g] Marta Granollers Mesa[a] and Amin Osatiashtiani *[f]

γ-Valerolactone (GVL) is a valuable bio-based chemical, solvent and fuel additive derived from levulinic acid, a key platform chemical from lignocellulosic biomass. Catalytic transfer hydrogenation (CTH) of levulinic acid using secondary alcohols as hydrogen donors presents a sustainable alternative to conventional hydrogenation with molecular hydrogen and can be efficiently carried out with inexpensive oxides. Here, we demonstrate how controlled silica incorporation onto zirconia provides a route to tailor acidity and thus direct reactivity in the CTH of levulinic acid and its esters to GVL. Silica-doped zirconia catalysts with varying Si loadings were synthesised *via* colloidal deposition and comprehensively characterised using ICP-OES, TEM/EDX, XRD, BET, NH_3-TPD, pyridine-adsorbed DRIFTS, XPS and NEXAFS. Moderate silica incorporation enhanced surface area, stabilised the tetragonal ZrO_2 phase, and increased total acidity, and most importantly, altered the Brønsted-to-Lewis acid balance that dictated the reactivity. Ethyl levulinate conversion was favoured over Lewis acid-rich catalysts, whereas LA conversion required higher Brønsted acidity. The optimal catalyst (6 wt% Si) delivered 80% GVL yield from levulinic acid at 190 °C in 4 hours. Isopropyl levulinate was identified as a side-product that can also convert to GVL *via* CTH, though less efficiently. The 6 wt% Si/ZrO_2 catalyst exhibited excellent stability across three consecutive cycles without calcination, demonstrating resistance to leaching, a major drawback of heterogeneous catalysts in liquid-phase reactions, as well as to carbon deposition. This study demonstrates that silica doping provides an effective means of tuning zirconia acidity, resulting in catalysts that combine good stability with practical applicability in sustainable chemistry.

Received 11th October 2025
Accepted 13th January 2026

DOI: 10.1039/d5ta08295a

rsc.li/materials-a

1 Introduction

The chemical industry produces nearly one billion tonnes of products each year, contributing to approximately 7% of global gross domestic product (GDP).[1,2] Its outputs ranging from plastics and fertilisers to pharmaceuticals and synthetic fibres, have played a central role in improving health, food security, and overall quality of life. However, this economic and societal importance comes with significant environmental impact. The sector remains one of the most energy-intensive and continues to rely heavily on fossil resources, with over 90% of chemical products still derived from them.[3] In 2020, direct emissions from petrochemical production were estimated at 1.30 Gt CO_2-equivalent, corresponding to roughly 14% of global industrial greenhouse gas emissions and about 2.5% of total anthropogenic emissions.[1] These figures reflect the scale of the challenge in cutting emissions across the chemical industry and point to the need for cleaner feedstocks and low-carbon technologies. To help reduce reliance on fossil-derived inputs, researchers and industries are increasingly turning to renewable carbon sources. Biomass, derived from lignocellulose, sugars, and triglycerides, is the only sustainable feedstock capable of supporting the large-scale production of fuels and chemicals.[4] Among these, lignocellulosic biomass stands out for its abundance, low cost, and lack of competition with food supplies, making it a particularly attractive option for sustainable chemical manufacturing.[5]

Among biomass-derived chemicals, γ-valerolactone (GVL) has attracted considerable attention due to its versatility. GVL can serve as a green solvent, fuel additive, and intermediate for

[a]Energy & Bioproducts Research Institute (EBRI), College of Engineering and Physical Sciences, Aston University, Aston Triangle, Birmingham, B4 7ET, UK
[b]Department of Chemistry, University College London, 20 Gower Street, London, WC1H 0AJ, UK
[c]HarwellXPS, Research Complex at Harwell, Rutherford Appleton Lab, Didcot, OX11 0FA, UK
[d]B07, Diamond Light Source, Rutherford Appleton Lab, Didcot, OX11 0DE, UK
[e]Chemical Process and Energy Resources Institute, Centre for Research and Technology Hellas, 6th km Harilaou-Thermi Road, 57001, Thessaloniki, Greece
[f]School of Chemical and Process Engineering, University of Leeds, Leeds, LS2 9JT, UK. E-mail: a.osatiashtiani@leeds.ac.uk
[g]Luxfer MEL Technologies, Manchester, M27 8LN, UK

polymers and bio-based chemicals and fuels. GVL has demonstrated strong potential as a safer alternative to conventional polar aprotic solvents. It is readily biodegradable and exhibits low toxicity to humans and aquatic organisms. Coupled with its comparable solvent properties to acetone, *N*-methylpyrrolidone, dimethylformamide and dimethylacetamide, GVL presents a strong case as a sustainable, multifunctional solvent across diverse chemical applications.[6] Apart from being safe and environmentally friendly, GVL has proven effective in biomass fractionation processes, enabling efficient separation of lignin and carbohydrates.[7–9] It also shows promise in emerging applications such as photocatalytic C–H bond activation, where its high dielectric constant and polarizability lower the activation barrier and enhance radical stabilisation, enabling efficient self-coupling of benzylic compounds under visible light.[10] GVL is also a promising fuel additive. Bereczky *et al.* demonstrated that blending 7% GVL with biodiesel and diesel reduced smoke emissions by up to 47% compared to neat diesel, with minimal impact on engine performance or NO_x emissions.[11] In a separate study, a 10% GVL blend in petrol was shown to deliver octane ratings comparable to those of ethanol.[12] GVL can also serve as an intermediate for the production of advanced biofuels and renewable chemicals. Through catalytic upgrading, GVL can be converted into valeric acid derivatives and further processed *via* hydrodeoxygenation to yield liquid alkanes suitable for use in diesel and jet engines,[13,14] offering a route to drop-in fuels from lignocellulosic biomass. In addition, GVL is a versatile precursor to valuable chemicals such as 2-methyltetrahydrofuran (MTHF), 1,4-pentanediol, and adipic acid which are key building blocks for green solvents and renewable monomers used in the production of nylons,[15] polyethers, and polyurethanes.[13]

GVL can be produced by hydrogenating bio-based levulinic acid (LA) or its esters. LA production has been commercialised by GF Biochemicals, who demonstrated scalable synthesis from biomass.[16] Traditional hydrogenation relies on high-pressure hydrogen gas and precious metal catalysts. Despite its widespread availability, hydrogen production from natural gas or water electrolysis is energy-intensive, raising sustainability and economic concerns. Catalytic transfer hydrogenation (CTH) is a promising alternative, using liquid hydrogen donors and avoiding precious metals and hazardous H_2.[17,18] CTH operates near thermoneutrality, requiring minimal energy with effective heat recovery.[19] Alcohols have shown promising results as hydrogen donors under mild conditions when combined with non-precious catalysts such as those based on Zr,[20–22] Ni,[23–26] and Cu,[27,28] as well as pure[29] and Zr-modified zeolites.[30–32]

Despite extensive research into CTH of LA and its esters, significant challenges remain in identifying catalysts that are highly active but also practically viable. Numerous catalysts reported in the literature demonstrate excellent activity and selectivity toward GVL but require complex synthesis routes. The synthesis of high-performance materials often involves multistep procedures, the use of expensive precursors (*e.g.*, as templating agent), or the incorporation of multiple active components such as bimetallic or trimetallic systems. These factors increase cost and hinder scalability, posing a barrier to commercial deployment. Therefore, the development of simple, cost-effective, and scalable catalysts with tunable properties remains a key challenge in advancing CTH as a sustainable route for GVL production.

In response to these challenges, there is growing interest in non-precious metal catalysts, particularly solid acid materials such as zirconia-based systems, which offer greater potential for scalable and commercially viable processes. Zirconia is thermally stable and relatively inexpensive. Although not strongly acidic in its native form, ZrO_2 has demonstrated tunable acidity with the ability to develop both Brønsted and Lewis acid sites, making it attractive for acid-catalysed reactions such as CTH.

The performance of catalysts in transfer hydrogenation of LA and esters is closely tied to the nature and balance of acid sites. Across multiple studies, an optimal combination of Lewis and Brønsted acid sites has been shown to improve activity and selectivity for GVL. For instance, ZrO_2/SBA-15 materials demonstrated highest GVL yields when a monolayer of ZrO_2 introduced a balanced distribution of Lewis and Brønsted sites, enabling carbonyl activation as well as cyclisation.[33] In another work, Soumoy *et al.* tested Zr-decorated silica nanostructures (hollow nanotubes and porous nanospheres) in ethyl levulinate conversion to GVL, revealing that morphology, structural/textural properties, and an optimal Lewis/Brønsted acid ratio govern the activity and stability of the catalysts.[34] Zirconium phosphate catalysts further confirmed that excess Brønsted acidity could suppress performance, with optimal GVL selectivity achieved at intermediate Brønsted/Lewis site ratios.[35] Additionally, sulphated zirconia, with strong Brønsted acidity, has been shown to promote esterification and lactonization steps in batch and continuous-flow CTH systems.[36] These findings collectively highlight the importance of acid site cooperativity, making control over the type and quantity of acid sites key to optimising GVL yield and selectivity using solid acid catalysts.

There are various methods to enhance and tune the acidity of ZrO_2. Sulphation, one of the most common methods, involves treating zirconia with sulphuric acid or other sulphate precursors, leading to the formation of surface SO_4 groups that increase Brønsted acidity.[37–40] Similarly, phosphation introduces phosphate species onto the zirconia surface, enhancing the density and strength of acid sites.[41,42] A common issue with sulphated and phosphated zirconia catalysts is poor stability due to the weak interaction between the sulphate or phosphate groups and zirconia that causes the leaching of functional groups, especially at high loadings.[43] Functionalisation with sulfonic acid groups provides additional Brønsted acidity through grafted $-SO_3H$ groups.[44–46] Tungstate doping can also enhance the acidity. It involves the dispersion of WO_x species onto zirconia, which can interact with surface hydroxyls and oxygen vacancies to generate strong acid sites.[47–49] The interaction between tungstate species and zirconia are generally stronger than sulphate–zirconia interaction, which to some extent addresses the catalyst stability issue. However, tungstated catalysts often lack the superacidity observed in sulphated zirconia. Additionally, although W is far less expensive than precious metals, it is significantly more costly than some

other abundant elements such as Al and Si. Zirconia combined with other metal oxides such as alumina,[50] titania,[51,52] or silica alters the electronic structure and surface properties. These additives are inexpensive and readily available, making the approach cost-effective. Additionally, they can enhance thermal and hydrothermal stability, improve textural properties (*e.g.*, surface area and porosity), making the resulting catalysts more suitable for industrial applications.

Silica in particular is an abundant and inexpensive oxide that has been shown to be able to enhance the acidity of zirconia-based catalysts, hence improving performance in acid-catalysed reactions. For example, Wang *et al.* demonstrated that flame-derived silica-zirconia exhibited markedly higher activity than pure zirconia in the one-step conversion of phenylglyoxal to ethyl mandelate, attributing this enhancement to the presence of Brønsted acid sites formed by silica incorporation.[53] Similarly, Scotti *et al.* investigated amorphous mixed Zr–Si oxide nanoparticles with strong Brønsted acidity. Their optimised material (ZrSi30) outperformed benchmark solid acids in the dehydration of 1-octanol, with superior activity, selectivity, and stability.[54] In a recent study, Zhao *et al.* reported that silica species leached from glassware during the synthesis of $Zr(OH)_4$ significantly modified the surface acid-base properties, leading to Zr–O–Si structures that enhanced the balance of Lewis and Brønsted acid sites for the CTH of LA to GVL, highlighting the critical role of silica incorporation albeit through an unintended route.[55]

Building on this concept, our work systematically incorporates silica into zirconia to explore its influence on the physicochemical properties and catalytic behaviour of the resulting materials. Owing to silica's abundance, low cost, and the feasibility of incorporating it into zirconia by simple, scalable methods, this approach holds promise for commercialisation applications. Despite these advantages, silica-zirconia remains comparatively less studied than other acid-modified systems, leaving ample scope for exploring its structure-acidity-performance relationships.

In this study, we synthesised a series of silica-zirconia catalysts with varying Si/Zr ratios *via* a straightforward surface modification method. The catalysts were evaluated in the catalytic transfer hydrogenation of LA and its esters to GVL, using 2-propanol as the hydrogen donor. The catalysts were characterised using elemental analysis, X-ray diffraction, surface area measurements, NH_3-TPD, and pyridine-DRIFTS to evaluate their physicochemical properties and acid site characteristics, as well as XPS and NEXAFS to probe the catalysts' surface and silicon environment. To the best of our knowledge, this represents the first systematic investigation of silica-doped zirconia materials in transfer hydrogenation reactions.

2 Experimental

2.1 Materials

Ethyl levulinate (EL, 98%), levulinic acid (LA, 98%), γ-valerolactone (GVL, 98%), 2-propanol (99.5%), and potassium bromide (99+%, IR grade) were purchased from Fisher Scientific, UK. Isopropyl levulinate (IPL, 99%) was acquired from Gute Chemie abcr, Germany. LUDOX® AS-30 colloidal silica (30 wt% suspension in H_2O), and *n*-dodecane (99%) were purchased from Sigma-Aldrich, UK. Zirconium hydroxide, $Zr(OH)_4$ (XZO1501/09) was provided by Luxfer MEL Technologies, UK.

2.2 Catalyst preparation

A series of silica doped zirconia (SiO_2/ZrO_2) catalyst with 1.5, 3, 6, and 10 wt% Si were prepared through a colloidal deposition method. To prepare each sample, zirconium hydroxide was immersed in denoised water at a 1 : 16 ratio (g of support: mL of H_2O) and stirred for 2 h. Then, an appropriate amount of LUDOX® AS-30 colloidal silica suspension, calculated based on the desired Si loading, was added to the zirconium hydroxide mixture and mixed thoroughly for 2 h at room temperature. Subsequently, the mixture was heated to 80 °C under constant stirring to evaporate the water. Finally, the samples were calcined in static air at 500 °C for 3 h, with a heating rate of 10 °C min^{-1} to obtain the SiO_2/ZrO_2 catalysts. The catalysts are denoted as *x*Si/Zr, where *x* represents the Si weight percent in the material. To obtain pure ZrO_2, the same zirconium hydroxide material was calcined following the same procedure as the rest of the catalyst series.

2.3 Catalyst characterisation

The catalysts' Si content was measured by Inductively Coupled Plasma-Optical Emission Spectroscopy (ICP-OES) performed by Medac Ltd using a Varian 720-ES system.

The surface areas and pore sizes of catalysts were measured by N_2 physisorption on a Quantasorb Nova 4000 instrument. Samples were degassed at 120 °C under vacuum for 4 h prior to analysis at −196 °C. The specific surface area was calculated by applying the Brunauer–Emmett–Teller (BET) model in the range of $P/P_0 = 0.03$–0.20, where a linear relationship was maintained. Pore size distributions were obtained using the Barrett–Joyner–Halenda (BJH) model applied to the desorption branch of the isotherm.

Powder X-ray diffraction (XRD) patterns were recorded on a Bruker D8 Advance diffractometer using Cu K_α radiation with crystalline phase identification performed in the range $2\theta = 20$–$80°$ with a step size of 0.04°.

Ammonia chemisorption followed by temperature-programmed desorption (NH_3-TPD) was conducted using approximately 0.15 g of catalyst, loaded into a fixed bed quartz reactor. The sample was pre-treated in helium at 500 °C for 40 min, then cooled to 100 °C under He flow. Ammonia adsorption was performed by flowing 5% NH_3/He over the sample for 1 h at 100 °C. To remove physiosorbed ammonia, the sample was purged with pure helium at 100 °C for 2 h. TPD was then conducted from 100 to 900 °C at a heating rate of 10 °C min^{-1} under a constant helium flow. The composition of the effluent gas was monitored online using a quadrupole mass spectrometer (Omnistar, Balzer). Quantification of desorbed ammonia was based on the $m/z = 15$ signal, which is less prone to interference from other species such as water ($m/z = 17$) and hydroxyl fragments ($m/z = 16$).

Diffuse reflectance infrared Fourier transform (DRIFT) spectra of pyridine-adsorbed catalysts were acquired using a Bruker VERTEX 80v spectrometer (Bruker, UK) equipped with an infrared source and mercury cadmium telluride (MCT/A) photon detector, operated at −196 °C. Spectra were recorded by averaging 64 scans with 4 cm^{-1} resolution. Prior to pyridine adsorption, the catalysts were outgassed under vacuum at 150 °C. Subsequently, pyridine was applied to the samples and allowed to adsorb for 5 min, after which excess physisorbed pyridine was removed by overnight treatment in a vacuum oven at 150 °C. For analysis, 50 mg of each catalyst was diluted with 450 mg of finely ground KBr to obtain a 10 wt% mixture. DRIFT spectra of the diluted samples were collected using a Praying Mantis High Temperature Reaction Chamber (Harrick Scientific, USA) at 150 °C to minimise any physisorbed moisture interference.

Transmission electron microscopy (TEM) was conducted on an FEI Titan^3 Themis G2 operating at 300 kV fitted with 4 Energy Dispersive X-ray spectroscopy (EDX) silicon drift detectors, multiple STEM detectors and a Gatan One-View CCD. TEM samples were prepared by dispersing the powder in methanol, with a drop placed on a holey carbon coated copper grid.

XPS data was acquired using a Kratos Axis SUPRA using monochromated Al kα (1486.69 eV) X-rays at 15 mA emission and 12 kV HT (180 W) and a spot size/analysis area of 700 × 300 μm. The instrument was calibrated to gold metal Au 4f (83.95 eV) and dispersion adjusted to give a binding energy (BE) of 932.6 eV for the Cu $2p_{3/2}$ line of metallic copper. Ag $3d_{5/2}$ line full width at half maximum (FWHM) at 10 eV pass energy was 0.544 eV. Source resolution for monochromatic Al Kα X-rays is ~0.3 eV. The instrumental resolution was determined to be 0.29 eV at 10 eV pass energy using the Fermi edge of the valence band for metallic silver. Resolution with charge compensation system on <1.33 eV FWHM on polytetrafluoroethylene (PTFE). High resolution spectra were obtained using a pass energy of 20 eV, step size of 0.1 eV and sweep time of 60 s, resulting in a line width of 0.696 eV for Au $4f_{7/2}$. Survey spectra were obtained using a pass energy of 160 eV. Charge neutralisation was achieved using an electron flood gun with filament current = 0.4 A, charge balance = 2 V, filament bias = 4.2 V. Successful neutralisation was adjudged by analysing the C 1s region wherein a sharp peak with no lower BE structure was obtained. Spectra have been charge-corrected to the main line of the carbon 1 s spectrum (adventitious carbon) set to 284.8 eV. All data was recorded at a base pressure of below 9×10^{-9} Torr and a room temperature of 294 K. Data was analysed using CasaXPS v2.3.19PR1.0. Peaks were fit with a Shirley background prior to component analysis.

Soft energy XANES (Near edge X-ray absorption fine structure – NEXAFS) data was collected at beamline VerSoX (B07) at Diamond Light Source, UK (photon energy range: 45–2200 eV). A 600 lines/mm plane grating monochromator with a CFF of 2.25 mm was used. Si K-edge (1820–1880 eV, 0.01 eV step) measurements were performed.

2.4 Catalytic tests

Catalytic transfer hydrogenation of EL, IPL and LA were carried out using 2-propanol as the hydrogen donor solvent in a 100 mL Parr autoclave reactor equipped with a glass liner and a magnetic stirrer. In each experiment, the reactor liner was charged with 5 mmol of a single reactant (EL, LA or IPL), 250 mmol (19.1 mL) of 2-propanol, 0.5 mmol (0.12 mL) of *n*-dodecane as an internal standard, and 100 mg of catalyst. A large excess of 2-propanol was used to ensure that the hydrogen donor was never rate-limiting. The reactor was then purged three times with nitrogen at atmospheric pressure and subsequently by pressurisation to 5 bar. The reaction mixture was then heated to 170 °C and stirred continuously at 600 rpm for 6 h. After the reaction, the reactor was cooled down to room temperature, and catalyst was separated from the reaction mixture by filtration. The filtrate was analysed using a gas chromatograph (GC2010, Shimadzu Instruments) equipped with a Zebron ZB-WAXPLUS column (30.0 m × 0.25 mm × 0.25 μm) and a flame ionisation detector (FID). Conversion, yield and selectivity were calculated using eqn (1)–(3),

$$\text{Conversion}(\%) = \frac{n_{s,i} - n_s}{n_{s,i}} \times 100 \quad (1)$$

$$\text{Yield}(\%) = \frac{n_p}{n_{s,i}} \times 100 \quad (2)$$

$$\text{Selectivity}(\%) = \frac{\text{Yield}}{\text{Conversion}} \times 100 \quad (3)$$

where n is the number of moles, s refers to substrate, i denotes the initial amount, and p stands for product.

Recyclability tests were performed following the same procedure as described above. After each run, the catalyst was recovered by filtration, washed thoroughly with fresh 2-propanol, and dried at 80 °C overnight before reuse.

Table 1 Physicochemical properties of SiO_2/ZrO_2 catalysts

Catalyst	Si loading[a]/wt%	Surface area[b]/m^2 g^{-1}	Total pore volume[c]/cm^3 g^{-1}	Total acidity[d]/μmol g^{-1}	B/L[e]
ZrO_2	0	89	0.55	128	0.2
1.5Si/Zr	1.5	188	0.63	199	0.5
3Si/Zr	3.2	221	0.66	212	0.6
6Si/Zr	6.1	290	0.71	270	0.7
10Si/Zr	9.9	269	0.61	178	1.6

[a] ICP-OES. [b] BET. [c] Measured at $P/P_0 = 0.99$. [d] NH_3-TPD. [e] Brønsted/Lewis (B/L) acid site ratio calculated from the integrated areas of pyridine adsorption bands at 1540 cm^{-1} (Brønsted acid sites) and 1447 cm^{-1} (Lewis acid sites) from pyridine/DRIFTS.

3 Results and discussion

3.1 Characterisation of SiO_2/ZrO_2 catalysts

ICP-OES analysis was undertaken to determine the bulk Si content of the catalysts after modification of zirconia support *via* the colloidal deposition method. The Si contents are presented in Table 1, showing that the measured loadings were close to the nominal values.

EDX mappings of the 3Si/Zr and 10Si/Zr samples (Fig. 1) shows how silicon distribution varies with increasing Si loading. At 3 wt% Si, the elemental maps show a uniform distribution of SiO_2 throughout the ZrO_2 particles. In contrast, the 10 wt% Si sample exhibits evident phase separation, with SiO_2 localised on the surface of the ZrO_2 particles. The main reason for this difference is most likely the use of a surface modification method for the synthesis of these materials. At low loadings, the SiO_2 particles in the precursor suspension can spread more evenly across the zirconia surface. However, as more silica is added, the surface becomes saturated, leading to the formation of SiO_2 overlayers, uneven distribution and formation of silica-rich phases.

The crystalline phase identification was carried out using XRD. As shown in Fig. 2, the XRD pattern of the parent ZrO_2 exhibits characteristic peaks at 24.3°, 28.2°, 31.5°, 34.4°, 35.2°, 38.6°, 40.7°, 45°, 49.3°, 50.2°, 54.1°, 55.5°, 60°, 62.8°, 65.7°, and 74.9° corresponding to the crystallographic planes of monoclinic zirconia (*m*-ZrO_2).[56] The tetragonal phase (*t*-ZrO_2) is typically identified by diffraction peaks at 30.2°, 50.2°, 50.7°, 59.3°, 60.1°, 62.8°, 73° and 74.5°.[57] However, most of these overlap with those of the monoclinic phase, except for the 30.2° peak, which is unique to the tetragonal phase with minimal interference from monoclinic reflections. This confirms that the parent ZrO_2 material comprises a mixture of monoclinic and tetragonal phases, which is typical for undoped zirconia calcined at 500 °C.[37] Upon addition of 1.5 wt% Si to zirconia, a clear change in the XRD pattern is observed. The 1.5Si/Zr catalysts exhibits diffraction peaks only at 30.2°, 34.6°, 50.5° and 60.2°, which are characteristic of *t*-ZrO_2. The stabilisation of the tetragonal phase and the absence of monoclinic peaks in this sample can be attributed to silica deposited on the surface of zirconium hydroxide during colloidal deposition. The silica likely acts as a physical barrier that inhibits crystallite growth by suppressing the sintering of zirconia particles during calcination. Since the phase transition from *t*-ZrO_2 to *m*-ZrO_2 is size-dependent,[58] the formation of nanoscale crystallites stabilises the tetragonal phase, which becomes more thermodynamically favourable than the monoclinic phase at small sizes due to its lower surface energy.[59] This can be rationalised in terms of the total Gibbs free energy of a crystallite, expressed as the sum of

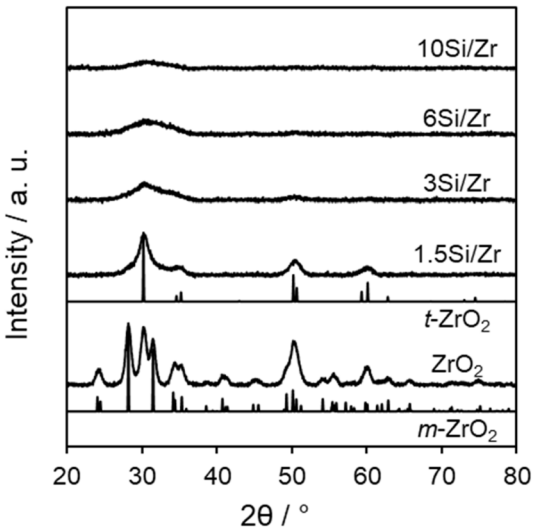

Fig. 2 XRD patterns of SiO_2/ZrO_2 catalysts with varying Si loadings calcined at 500 °C.

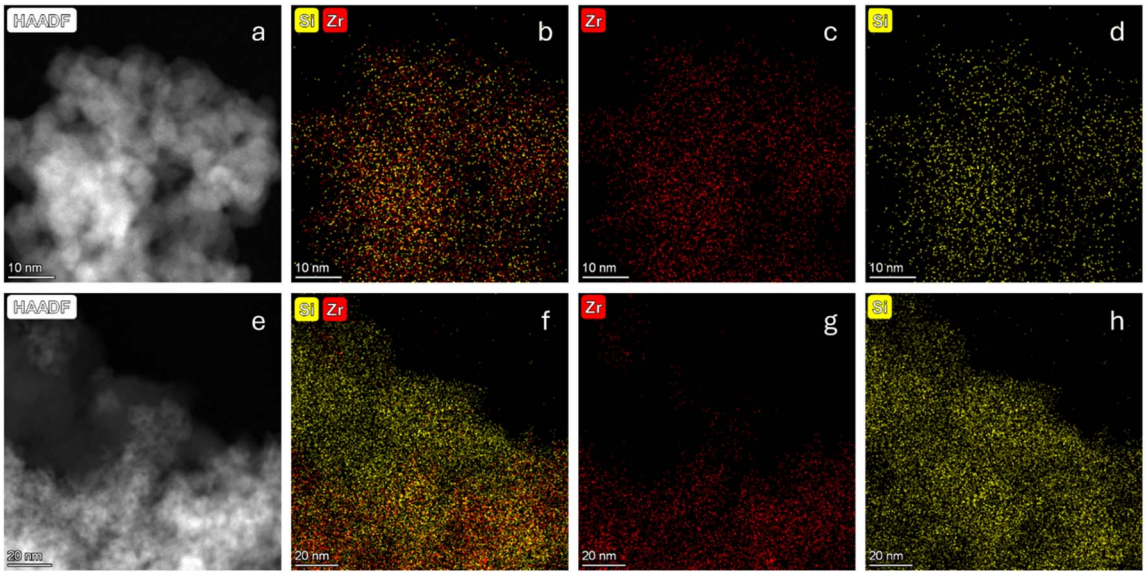

Fig. 1 STEM-EDX elemental mapping of (a–d) 3Si/Zr, and (e–h) 10Si/Zr.

bulk and surface contributions ($G_{total} = G_{bulk} + G_{surface}$). As particle size decreases, the surface-to-volume ratio increases, making $G_{surface}$ a larger fraction of the total free energy. At the nanoscale, where surface energy dominates, the tetragonal phase is stabilised because it has a lower surface energy than the monoclinic phase, resulting in a smaller G_{total}.[60] This observation is consistent with what has been previously reported on the stabilisation of *t*-ZrO_2 in SiO_2/ZrO_2 material.[61] At higher Si loadings, broadening of the tetragonal peaks is observed, indicating progressive reduction in crystallite size. Calculations using the Scherrer equation from the tetragonal (50.5°) reflection show crystallite sizes decreasing from ~65 nm for pure ZrO_2 to 56 nm and 46 nm for the 1 wt% and 3 wt% Si samples, respectively. For the 6 and 10 wt% Si samples, crystallite sizes could not be determined due to excessive peak broadening, suggesting extremely small crystallites below the instrument detection limit of 2–3 nm. This suggests that at higher Si loadings, surface silica disrupts atomic rearrangement during calcination, inhibiting the growth of well-defined crystallites and driving the material towards an amorphous structure.

TEM image of the parent ZrO_2 (Fig. 3a) reveal particles of varying sizes and shapes, with well-defined lattice fringes clearly visible, confirming the highly crystalline nature of the material, consistent with the XRD results. The observed particles typically range in size between 10 and 20 nm. These values are smaller than the average crystallite size estimated using the Scherrer equation, as expected, it is known that using *K* values close to unity *e.g.*, 0.9 by FWHM or 1.05 by integral breadth (IB) tends to overestimate crystallite size.[62] With the addition of 3 wt% Si, a noticeable change in morphology is observed. The TEM image of 3Si/Zr (Fig. 3c) show smaller crystallites that are connected by the amorphous SiO_2 network, leading to agglomeration (see enlarged Fig. S1 in the SI for clarity). This observation aligns with XRD data, which indicate a reduction in crystallite size and overall crystallinity at intermediate Si loadings. The individual ZrO_2 particles that were distinguishable in the parent ZrO_2 sample are embedded within and "glued together" by the SiO_2 matrix. At the highest Si loading (10 wt%), TEM image (Fig. 3e) reveal only unclear traces of crystalline domains, with those few visible crystallites appearing even smaller than in the 3 wt% sample (see enlarged Fig. S2 in the SI for clarity). The high degree of silica coverage results in a substantial loss of visible crystallinity. The evolution of crystallinity is further evidenced by selected area electron diffraction (SAED). The parent ZrO_2 exhibits a distinct diffraction pattern (Fig. 3b), confirming its high crystallinity. The sharp, bright spots corresponding to constructive interference from crystalline planes of ZrO_2, consistent with the TEM image and XRD analysis. As the Si loading increases to 3 wt%, the SAED pattern (Fig. 3d) shows weaker but still recognisable diffraction rings, indicating a reduction in crystallinity while retaining some ordered domains. At 10 wt% Si loading (Fig. 3f), the halo patterns become more evident, confirming a further reduction in crystallinity and formation of a predominantly amorphous material.

As mentioned earlier, the addition of SiO_2 to ZrO_2 led to the formation of agglomerated particles and reduced crystallinity.

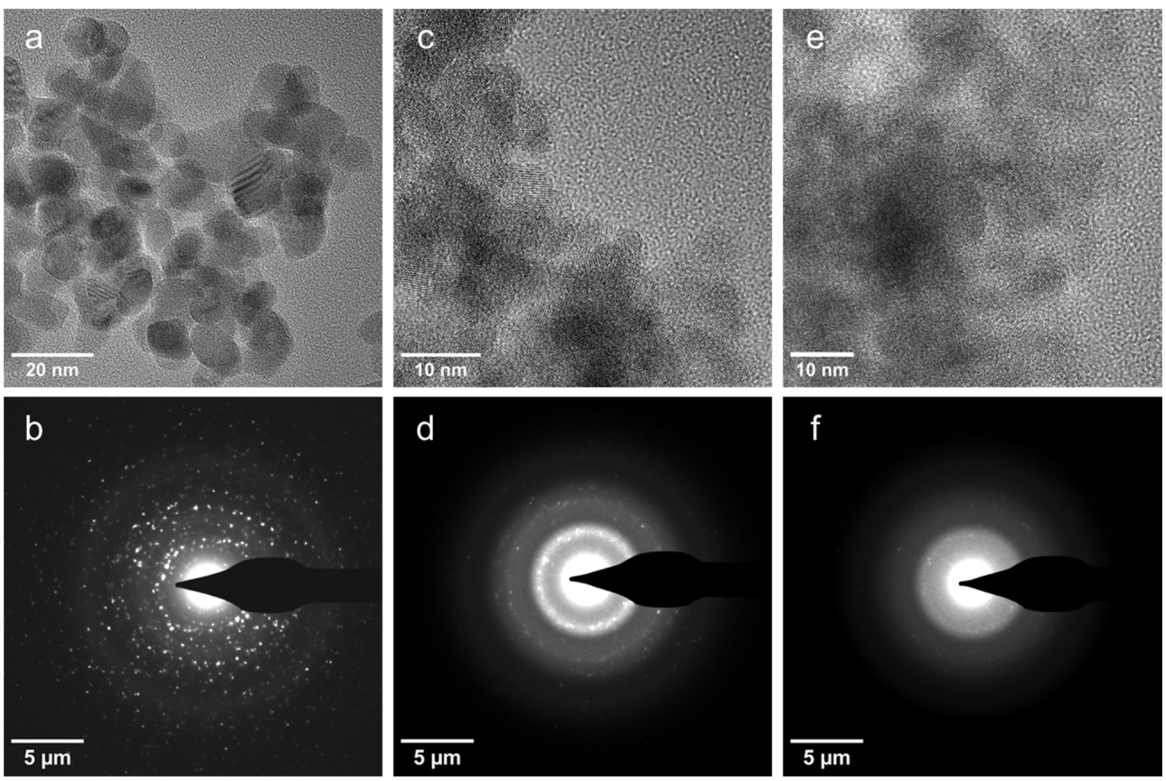

Fig. 3 TEM images and selected area electron diffraction for (a and b) ZrO_2, (c and d) 3Si/Zr, and (e and f) 10Si/Zr.

While agglomeration typically reduces surface area by decreasing external surface, amorphisation can have the opposite effect by introducing structural disorder and porosity. To understand how these structural changes affect the textural properties of the SiO_2/ZrO_2 materials, N_2 porosimetry was performed. As demonstrated in Fig. S3, isotherms of all samples exhibit a hybrid character, displaying features of both Type II and Type IV isotherms. The gradual uptake at low to intermediate relative pressures suggests multilayer adsorption on external surfaces, characteristic of Type II behaviour. At higher relative pressures (P/P_0 > 0.8), a sharp increase in adsorption and the presence of an H3-type hysteresis loop indicate capillary condensation in mesopores, typical of Type IV isotherms. This combination suggests a material structure composed of macro-size interparticle voids as well as mesopores, which is also reflected in the pore size distribution, as illustrated in Fig. S4. The corresponding surface area values, shown in Table 1, increased markedly from 89 $m^2\ g^{-1}$ for pure ZrO_2 to a maximum of 290 $m^2\ g^{-1}$ at 6 wt% Si. Additionally, the total pore volume increased from 0.55 to 0.71 $cm^3\ g^{-1}$ over the same range. This trend suggests that the effect of amorphisation dominates over agglomeration. At 10 wt% Si, both surface area and pore volume decrease slightly to 269 $m^2\ g^{-1}$ and 0.61 $cm^3\ g^{-1}$, respectively. This may be attributed to excessive silica coverage, where agglomeration becomes the dominant effect and/or where partial pore blockage occurs.

The surface acidity of the SiO_2/ZrO_2 catalysts was quantitatively assessed using temperature-programmed desorption of ammonia (NH_3-TPD), with the acid site loadings reported in Table 1. The incorporation of SiO_2 onto ZrO_2 resulted in a linear increase in acidity, from 128 μmol g^{-1} for the parent ZrO_2 to 270 μmol g^{-1} for the 6Si/Zr sample. This enhancement can be attributed to the formation of bridging Zr–O–Si bonds, which generate additional acid sites.[63–66] However, at the highest silica loading (10Si/Zr), the acidity decreased to 177 μmol g^{-1}, likely due to complete surface coverage by silica and the formation of Si–O–Si domains, which suppress Zr–Si interactions and diminish the overall acidic character.[67] Furthermore, as displayed in Fig. 4, the NH_3-TPD profiles reveal that the majority of ammonia desorbs below 400 °C. Typically, NH_3 desorption below 250 °C is attributed to weak acid sites, between 250–400 °C to intermediate acid sites, and above 400 °C to strong acid sites.[68] This indicates that the surface acidity in all samples is primarily composed of weak and intermediate-strength acid sites. Additionally, the desorption temperature remains largely unchanged across the series, suggesting that the acid strength is not significantly influenced by increasing Si content.

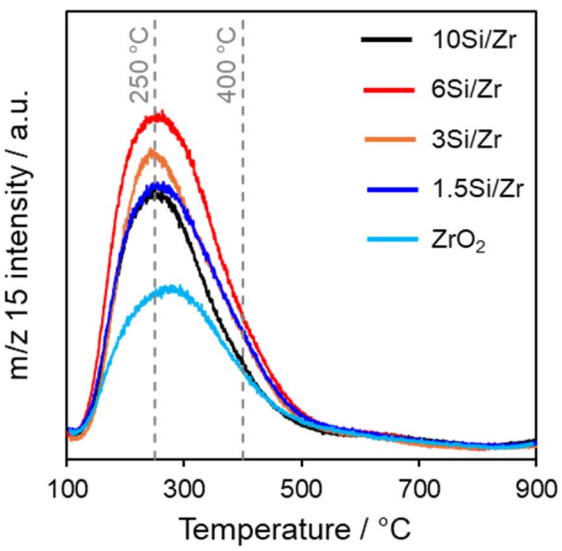

Fig. 4 NH_3-TPD profile of SiO_2/ZrO_2 catalysts with varying Si loadings, illustrating the intensity of *m*/*z* 15 (NH fragment) as a function of temperature.

Furthermore, pyridine/DRIFTS was performed on the SiO_2/ZrO_2 samples to determine the Lewis and Brønsted nature of the acid sites. The DRIFT spectra of pyridine adsorbed samples are shown in Fig. S5, exhibiting transmittance bands at wavenumbers of 1447 cm^{-1}, and 1540 cm^{-1}, corresponding to Lewis and Brønsted acid sites, respectively. An additional broader band is also observed at 1489 cm^{-1}, which is associated with pyridine interacting with both Lewis and Brønsted acid sites.[69,70] Through the integration of the bands at 1447 cm^{-1} and 1540 cm^{-1}, the quantity of Lewis and Brønsted acid properties was compared. Fig. 5 shows the variation in Lewis and Brønsted acid site densities across the SiO_2/ZrO_2 catalysts with different Si loadings. The acid sites of the parent ZrO_2 is mostly of Lewis acid character, likely originating from uncoordinated Zr^{4+} species.[71] Additionally, it can be observed that the Brønsted acidity increases steadily with increasing Si content. In contrast, Lewis acidity increases initially, reaching a maximum at 3 wt% Si, and then declines at 10 wt% Si. This trend mirrors that of the total acidity observed in NH_3-TPD measurements. As shown in Table 1, all catalysts except 10Si/Zr remain predominantly Lewis acidic, with Brønsted:Lewis acid site ratios <1. These observations are consistent with those reported by Miller and Ko,[63] who demonstrated that SiO_2/ZrO_2 mixtures develop new acid sites attributed to new Zr–O–Si linkages, with SiO_2-rich compositions favouring Brønsted acidity and ZrO_2-rich mixtures becoming Lewis acidic. It is worth noting, unlike Miller and Ko who used a sol–gel method for synthesising SiO_2/ZrO_2 materials, our catalysts were prepared by surface modification *via* colloidal deposition. This difference in synthesis approach likely explains the observed decline in acidity at high Si loadings, as silica gradually saturates the ZrO_2 surface. The decline in Lewis acidity at high Si content is supported by TEM-EDX mapping (Fig. 1), which shows that at 10 wt% Si, silica forms a continuous overlayer on ZrO_2, covering the surface of ZrO_2 and hence blocking Zr^{4+} sites responsible for Lewis acidity. Consequently, Lewis acidity declines whereas Brønsted acidity continues to increase because it originates from Si–OH groups that are located in close proximity of Lewis acid sites.[72]

XPS analysis was performed to quantify of the surface composition of the catalysts and compare it with the bulk values. In all cases, XPS reported a higher Si content than the bulk, consistent with the suggestion of Si depositing on the surface of these materials, while the overall trend reported a linear surface : bulk ratio (Table 2). XPS spectra were

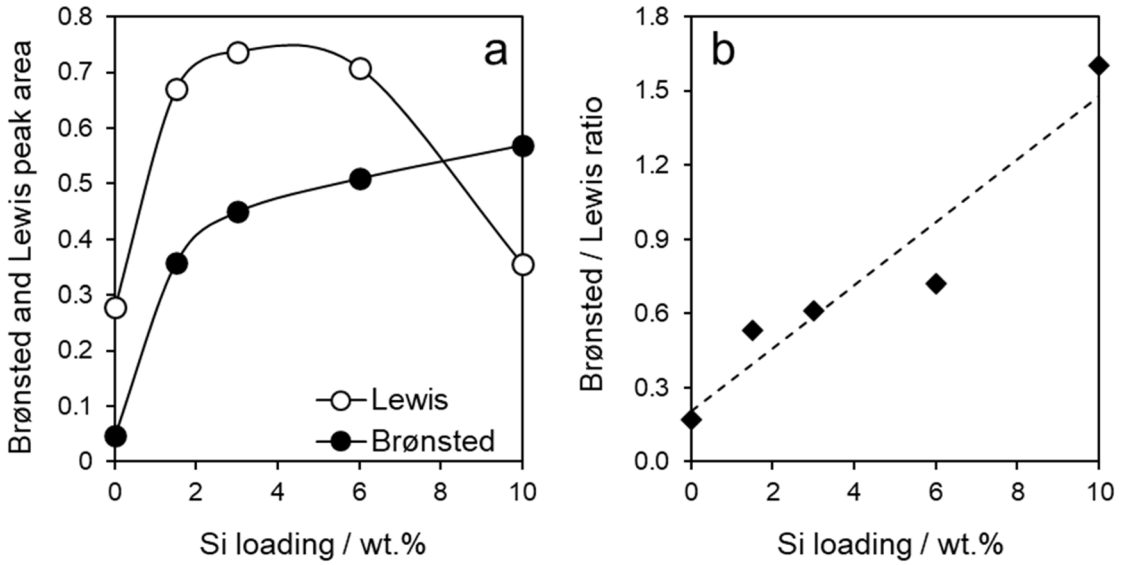

Fig. 5 Brønsted (1537 cm^{-1}) and Lewis (1444 cm^{-1}) acid sites peak area from pyridine/DRIFTS *versus* Si loading of the SiO_2/ZrO_2 catalysts.

Table 2 Surface composition of SiO_2/ZrO_2 materials obtained by XPS

	Surface loading/ at%				Surface loading/ wt%		
Catalyst	Zr	Si	O	Si/Zr atomic ratio	Zr	Si	O
ZrO_2	35.8	0.0	64.2	0.00	76.1	0.0	23.9
1.5Si/Zr	29.7	5.2	65.1	0.18	69.5	3.8	26.7
3Si/Zr	28.6	6.4	65.0	0.22	68.1	4.7	27.2
6Si/Zr	19.0	16.7	64.3	0.88	53.6	14.6	31.9
10Si/Zr	11.1	24.9	64.0	2.25	37.0	25.6	37.4

calibrated to adventitious carbon at 284.8 eV, although this procedure may be considered slightly erroneous in the case of oxides with large degrees of difference in acidity, and as such absolute binding energy values were treated with caution.[73,74] Instead, energy differences were investigated to reveal trends in the sample environment, with the energy separation between Zr 3d, and Si 2p photoelectrons ($\Delta E_{(Zr-Si)}$) found to increase with Si content (Fig. 6a), indicating that there is an increase in the relative dipole between Si and Zr, consistent with the formation of Si–O–Zr moieties, as electronegativity effects induce dipole changes in next-nearest neighbouring atoms.[75] Oxygen 1s was deconvoluted (Fig. 6b) using the pure ZrO_2 as a reference, revealing a lattice oxygen and a surface oxygen largely comprised of hydroxyls,[76] while the O KLL regions were analysed through generation of a line shape from reference data (Fig. 6c), and using non-linear least squares fitting to determine shifts in major emission energy and peak area, similar to methods used in literature.[77] Following deconvolution, $\Delta E_{(Zr-O)}$, and $\Delta E_{(Si-O)}$ could be identified (Fig. S6a), with both the Si and Zr components of the system reporting an affectation by increased loading, indicating that the change to $\Delta E_{(Zr-Si)}$ is indeed a commonality, and not the result of one species changing relative to the other. Veracity of the O 1s fit was determined using correlation analysis of the O 1s fits, which gave good agreement in both cases (Fig. S6b).[78] Finally, we could look at the individual Auger parameters for the Zr and Si components within the mixed system (Fig. 6d), observing a decreasing Auger parameter with increasing silicon for Zr and Si components, indicating reduced polarizability as we increase Si content. This again is consistent with the suggestion of formation of Si–O–Zr bonds, since Si atoms are smaller and less polarizable. O KLL : KLV ratios and differences are also in agreement with this observation (Fig. S6c).[79]

XPS spectra also gave insights into the spatial configuration of the moieties of this system (Fig. 6e), with the inelastic photoelectron background of the lowest kinetic energy Zr peaks (3p and 4s) revealing marked differences for the pure zirconia *versus* the silicon modified system. After addition of silicon in the maximum loading, the post peak background (normalised to Zr peak area) sees a large rise, due to inelastic scatter from an overlayer (in this case silica).[80] Analysis of the peak area ratio between the Zr 4s peak (~1040 eV kinetic energy), and the Zr 3s peak (~1400 eV kinetic energy) reveals a trend of increasing Zr 4s proportion with Si content. TPP2M calculations determine the inelastic mean free path (IMFP) of Zr 4s photoelectrons through silica to be 3.85 nm, while for Zr 3s photoelectrons, this is around 3 nm, again supporting the earlier assertions of a silica overlayer given this changing ratio indicates an overlayer (Fig. 6f).

Si K-edge NEXAFS (Fig. S6d) was used to probe the silicon environment, with the white line (representing the Si 1s → t_2(Si $3p_{x,y,z}$) transition) energy (E_{MAX}) found unchanged depending on silicon loading, which confirms the silicon is only bound to oxygen atoms.[81]

3.2 CTH of levulinic acid and esters

As demonstrated by catalyst characterisation, varying the Si doping level significantly affects the textural properties (*e.g.*,

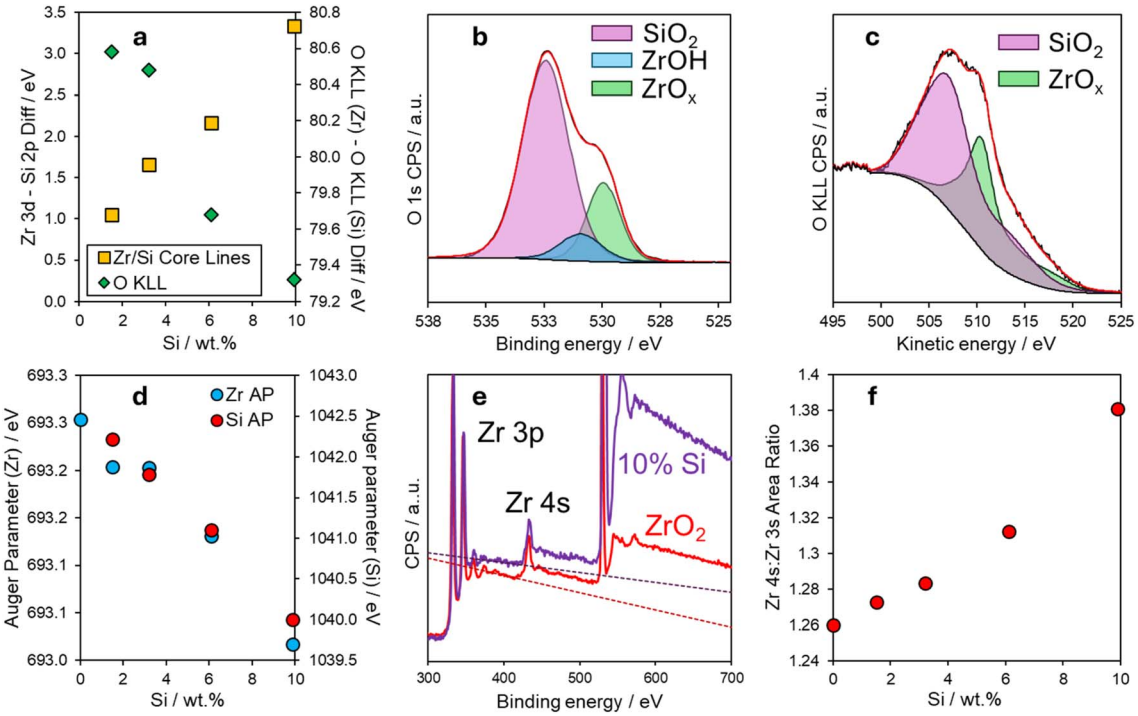

Fig. 6 (a) O 1s deconvolution, and (b) O KLL deconvolution of XPS spectra, (c) O KLL auger parameters for deconvoluted Si and Zr components, (d) binding and kinetic energy separations between Si 3d and Si 2p core lines, and the individual O KLL contributions from Zr and Si species, (e) selected energy range XPS survey scan highlighting post Zr 3p region, and (f) peak area ratio of Zr 4s : Zr 3s photoelectron peaks of SiO_2/ZrO_2 catalysts.

surface area), as well as the crystallinity and acidity of silica-doped zirconia. These changes can, in turn, influence the material's catalytic behaviour. Therefore, a systematic study of Si doping levels (Si wt% on ZrO_2) was conducted to assess their effect on catalyst activity, selectivity, and overall performance in the CTH reactions of EL and LA.

Initially, the catalytic performance of SiO_2/ZrO_2 materials with different Si loadings was evaluated in the transfer hydrogenation of EL using 2-propanol as the hydrogen donor solvent at 170 °C. As shown in Fig. 7a, under these conditions, the pure ZrO_2 support achieved an EL conversion of 53% and a GVL yield of 48%, after 6 h. As the Si loading increased from 0 to 3 wt%, EL conversion and GVL yield increased, reaching a maximum of 78% and 68%, respectively. However, the conversion and yield decreased upon further addition of silica.

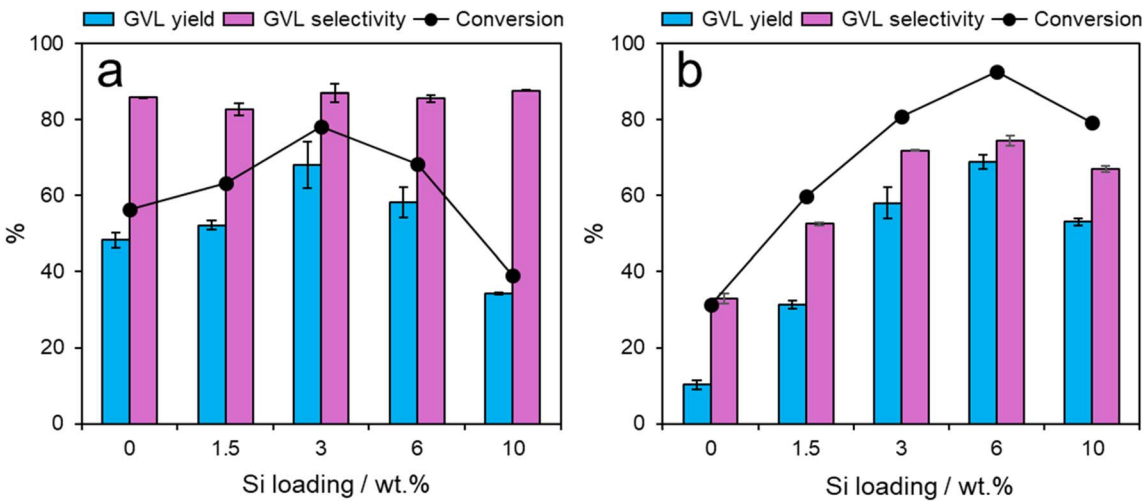

Fig. 7 Catalytic performance of SiO_2/ZrO_2 series with varying Si loading in transfer hydrogenation of (a) EL, and (b) LA. Reaction conditions: catalyst (100 mg), EL or LA (5 mmol), 2-propanol (250 mmol), internal standard (*n*-dodecane, 0.5 mmol), 5 bar N_2, 170 °C, 6 h.

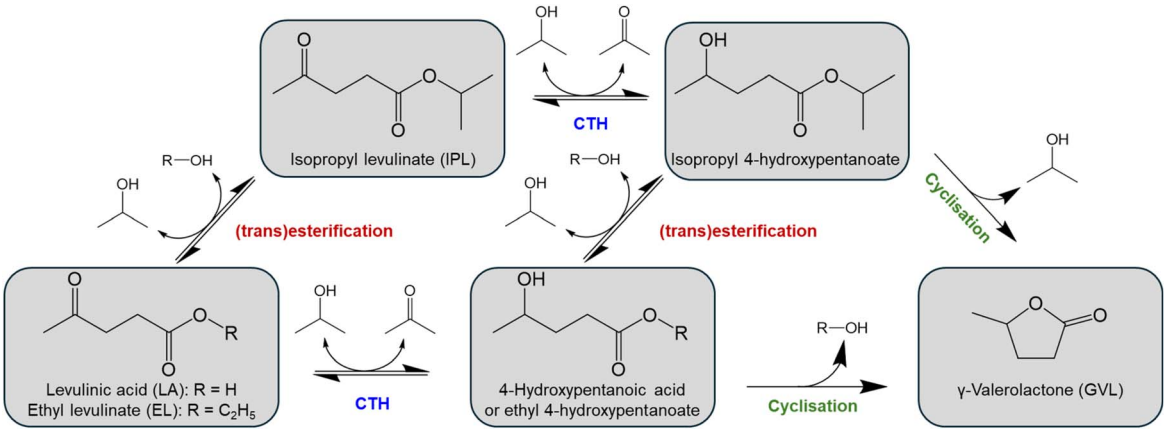

Fig. 8 The widely accepted reaction pathways for the liquid phase CTH of levulinic acid and ethyl levulinate using 2-propanol as a hydrogen donor.[20,23,33,36]

GVL selectivity remained consistently high (~85%) across all samples, with only minor variations.

This behaviour can be explained by the combined effects of acidity and textural properties, both of which are influenced by Si doping. Consistent with earlier mechanistic studies, the hydrogenation of EL, facilitated by Lewis acid sites, leads to the formation of 4-hydroxypentanoic acid ester as an intermediate product (Fig. 8). This intermediate will undergo cyclisation to GVL which proceeds *via* a Brønsted acid-catalysed lactonisation.[82–86] Among the different physicochemical factors that can influence the catalytic performance, the trend in conversion and GVL yield most closely follow the concentration of Lewis acid sites, highlighting their central role in the initial CTH step. As evidenced by the characterisation data (Fig. 5a), moderate Si incorporation maximises Lewis acidity and also increases surface area and maintains a sufficient Brønsted contribution to promote the cyclisation step and the trans-esterification route. However, it is worth noting that when the Si loading increased from 0 to 1.5 wt%, only a moderate increase in EL conversion (~7%) was observed, while the number of Lewis acid sites more than doubled. A plausible explanation for this disproportionality may be related to the nature of the initial transfer hydrogenation step. The transfer hydrogenation step (EL → ethyl 4-hydroxypentanoate) is catalysed by Lewis acid sites, however this step is known from the literature to proceed through a reversible Meerwein–Ponndorf–Verley (MPV) hydride-transfer mechanism.[87–89] Because this reaction is reversible, increasing the number of Lewis acid sites alone does not necessarily translate into a proportional increase in net conversion unless the downstream steps efficiently remove or transform the intermediate. At 1.5 wt% Si, the large increase in Lewis acidity did not lead to a proportional increase in EL conversion most likely because the subsequent Brønsted-acid-catalysed cyclisation of ethyl 4-hydroxypentanoate is not yet fast enough to pull the MPV equilibrium forward. At this loading, the Brønsted acidity has not yet reached optimal level, so the additional Lewis sites are not fully translated to higher conversion. As a result, the equilibrium can shift backwards, limiting the apparent disappearance of EL even when more Lewis sites are present. In contrast, the catalyst with 3 wt% Si provides a more favourable combination of Lewis and Brønsted acidity, which allows the intermediate to be consumed more rapidly and pulls the equilibrium forward. Therefore, a greater increase in conversion is observed at 3 wt% Si, even though the increase in Lewis acidity is smaller. At 6 wt% Si loading, the number of Lewis acid sites decreases but Brønsted acidity

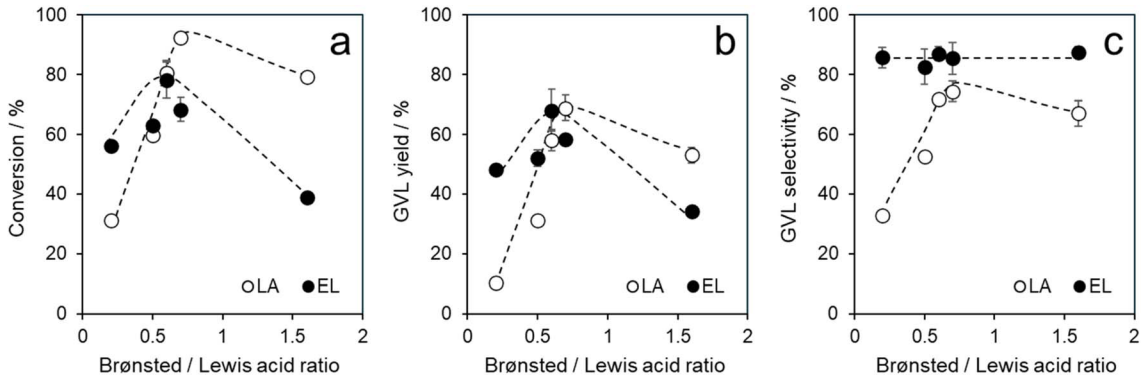

Fig. 9 Effect of varying Brønsted/Lewis acid ratio on the conversion of EL and LA.

continues to increase, leading to a higher Brønsted/Lewis (B/L) ratio. Under these conditions, the MPV hydrogen-transfer step becomes limited by the reduced number of Lewis sites, and the overall conversion decreases accordingly. However, the corresponding decrease in overall EL conversion is not proportional to the loss of Lewis sites. This could be explained in terms of the Brønsted-acid-catalysed transesterification of EL to IPL (Fig. 8). This pathway partially compensates for the reduced hydrogen-transfer activity, so the drop in EL conversion is smaller than the drop in Lewis acidity. At 10 wt%, the number of Lewis acid sites decreases significantly, leading to a substantial decrease in conversion.

A similar set of experiments was conducted using LA as the reactant under identical conditions. The transfer hydrogenation of LA also exhibited a strong dependence on Si loading. As shown in Fig. 7b, pure ZrO_2 exhibited modest activity, achieving 31.3% conversion and a GVL yield of 10.3%. Incorporation of silica markedly enhanced performance, with conversion increasing steadily with Si loading and reaching a maximum of 91% at 6 wt% Si. A similar trend was observed for GVL yield, which peaked at 67.4% at this composition. At higher loading (10 wt% Si), both conversion and yield declined, though performance remained significantly higher than that of undoped ZrO_2 (79.2% conversion, 53% yield).[24,25]

The difference in reactivity between EL and LA arises from the inherent properties of their carbonyl groups. As shows in Fig. 9, at low B/L ratios (low Si loading), EL is more reactive than LA, likely because the ester carbonyl of EL is intrinsically more electrophilic and more readily activated to undergo CTH by Lewis acid sites than the carboxylic acid carbonyl of LA. This trend is also reflected in GVL yield, consistent with literature reporting that EL undergoes Lewis-acid-driven CTH more readily than LA.[90] Incorporating SiO_2 onto ZrO_2 introduces Brønsted acidity (as previously discussed), which narrows the reactivity gap between EL and LA in terms of conversion and GVL yield. The presence of Brønsted acid sites enables the transesterification of EL or esterification of LA. Both reactions produce IPL, which was identified as the only by-product in this study. At a B/L ratio of 0.6, EL and LA conversions become comparable (78% and 81%, respectively), although GVL yield from EL remains ~10% higher, indicating a more selective transformation. At a B/L ratio of 0.7 and above, LA conversion and GVL yield surpass those of EL. This suggests that the esterification of LA contributes more effectively to GVL production than EL transesterification under these conditions, compensating for LA's intrinsically lower direct CTH activity. Overall, as B/L ratios increases LA benefits more than EL because LA undergoes Brønsted-acid-catalysed esterification to IPL more readily than EL undergoes transesterification. GVL selectivity remains consistently lower for LA than for EL across all B/L ratios. This can be explained by the preferential esterification of LA over Brønsted acidic SiO_2-doped catalysts towards IPL, which competes with the desired CTH route and diverts a significant portion of LA away from it. Although IPL can undergo CTH over Lewis acid sites followed by Brønsted acid-catalysed cyclisation to form GVL, this tandem pathway appears to be less efficient. In contrast, EL undergoes direct CTH more readily, resulting in higher GVL selectivity and less IPL formation.

To further explore the role of B/L acid site balance and intermediate product reactivity, catalytic tests were conducted using IPL as the starting reactant, alongside EL and LA for comparison. As shown in Fig. 10a, IPL consistently exhibits the lowest conversion across all Si loadings, indicating its lower reactivity under the applied CTH conditions. Unlike EL, which can undergo transesterification in the presence of 2-propanol, IPL lacks this pathway since the leaving and incoming groups are both isopropyl, effectively precluding transesterification.

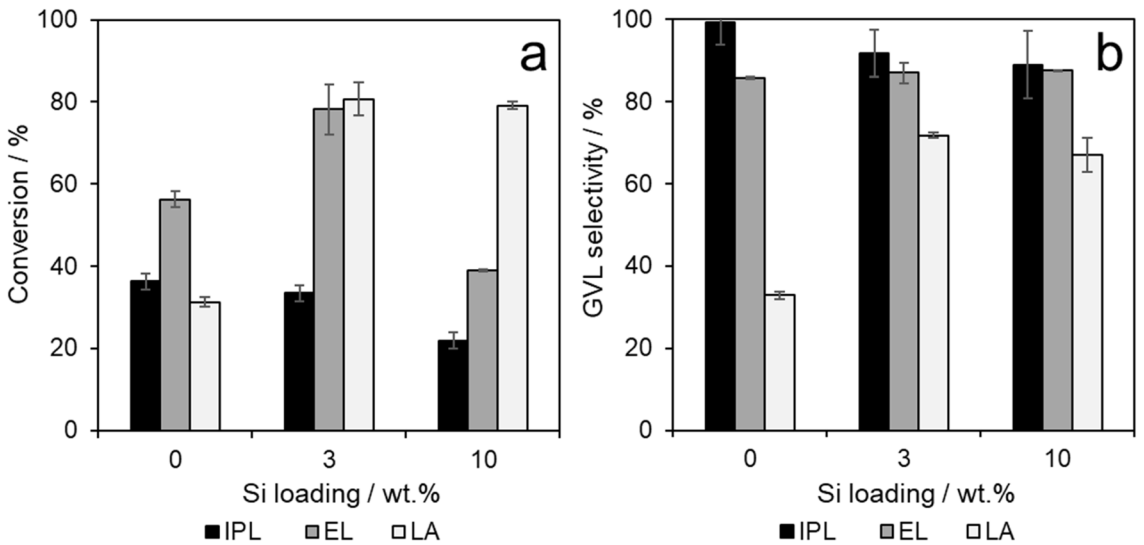

Fig. 10 Reactivity of IPL, EL and LA under CTH conditions. (a) IPL, EL and LA conversion, (b) GVL selectivity from IPL, EL and LA using Si/Zr catalysts. Reaction conditions: catalyst (100 mg), IPL, EL or LA (5 mmol), 2-propanol (250 mmol), internal standard (*n*-dodecane, 0.5 mmol), 5 bar N_2, 170 °C, 6 h.

Consequently, the primary route available to IPL is CTH. IPL's low reactivity likely arises from a combination of steric and electronic effects. The bulkier isopropyl group may impose greater steric hindrance, resulting in reduced access to active sites compared to LA and EL. Additionally, the isopropyl group exerts a stronger electron-donating inductive effect than the ethyl group of EL, increasing electron density at the carbonyl carbon and reducing its electrophilicity. This makes the carbonyl in IPL less susceptible to hydride transfer during CTH.[91] IPL conversion remained around 35% at 0 and 3 wt% Si loading but dropped to 22% at 10 wt% Si, likely due to diminished Lewis acidity in the 10Si/Zr catalyst. As shown in Fig. 10b, higher GVL selectivity was achieved from IPL compared to EL and LA at all Si loadings. This can be attributed to the limited number of side reactions IPL can undergo, unlike EL and LA, which are prone to (trans)esterification. Overall, while IPL can be converted to GVL, it is a less efficient route compared to direct CTH of EL or LA.

The influence of reaction time on the catalytic behaviour of EL and LA further supports the proposed reaction pathways. As presented in Fig. 11, EL and LA show increasing conversion and GVL yield over time. For both EL and LA, IPL yield progressively increases with time; however, significantly more IPL is produced from LA than from EL throughout the reaction. Likewise, IPL selectivity is consistently higher in reactions starting from LA. These observations are in agreement with the earlier conclusion that esterification of LA to IPL is a major competing pathway and occurs more readily than the transesterification of EL. Interestingly, across both reactants, IPL selectivity is highest at early times and then declines, suggesting

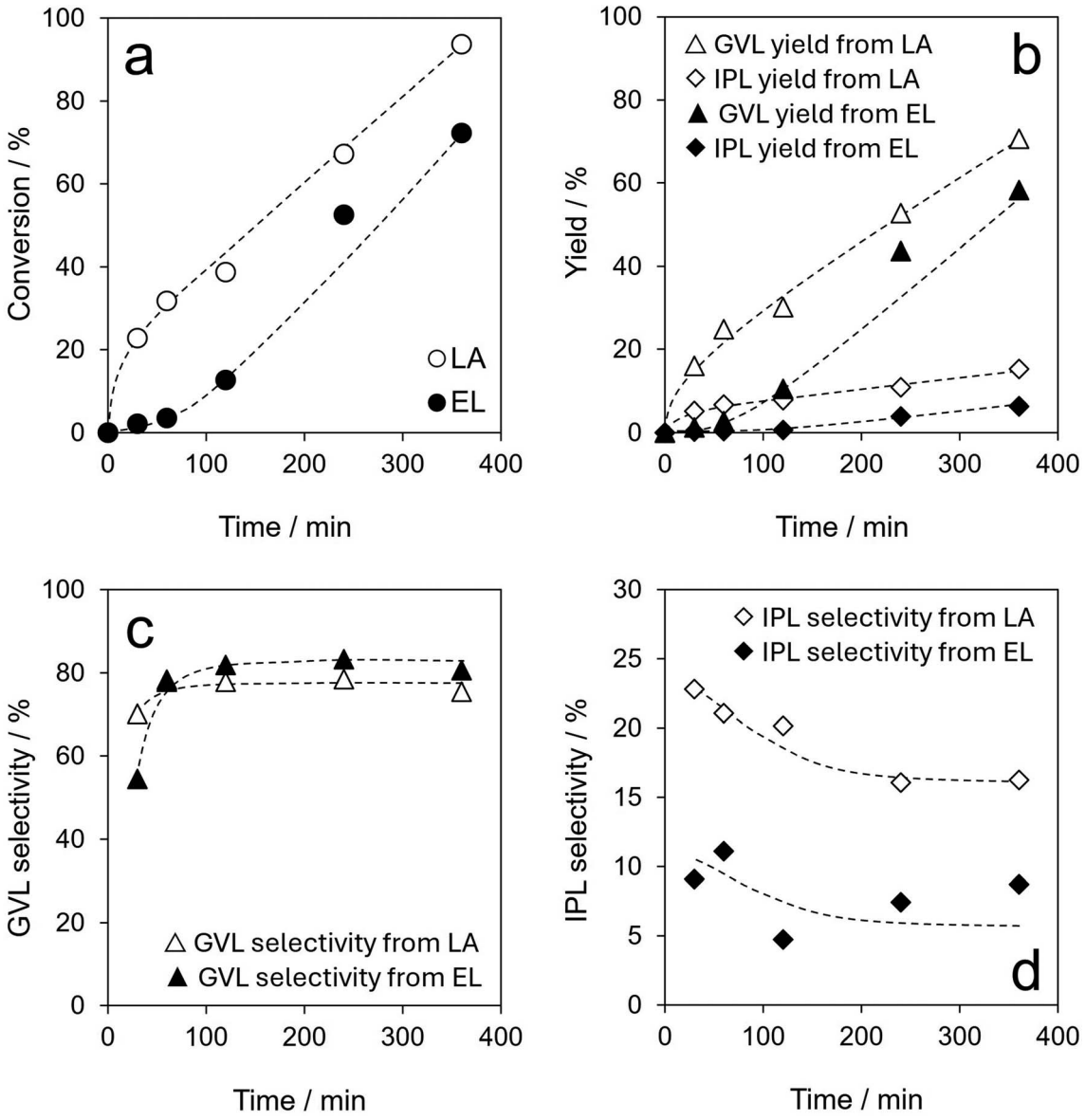

Fig. 11 Profiles of LA and EL conversion as well as GVL and IPL yield and selectivity. Reaction conditions: 6Si/Zr (100 mg), LA or EL (5 mmol), 2-propanol (250 mmol), internal standard (*n*-dodecane, 0.5 mmol), 5 bar N_2, 170 °C, 6 h.

that IPL behaves as a reaction intermediate rather than a terminal byproduct. The decrease in the selectivity is consistent with IPL being formed transiently and subsequently consumed, most likely *via* CTH to GVL. These observations support the idea that the (trans)esterification route diverts reactants from the direct CTH pathway and instead represents a secondary route in which IPL serves as an intermediate that can be converted to GVL under appropriate acid site conditions, albeit more slowly.

The influence of reaction temperature on EL conversion was systematically investigated using 6Si/Zr across a temperature range of 160–190 °C. All experiments maintained consistent reaction parameters, including reactant/catalyst ratio, solvent volume, and a fixed 6-hour duration, to enable direct comparison of temperature effects. As demonstrated in Fig. S7, EL reaction exhibited a strong temperature dependence, with conversion and GVL yield increasing significantly at elevated temperatures. At 190 °C, near-complete EL conversion (94%) was achieved, accompanied by an 83% GVL yield. IPL yield shows a clear temperature-dependent trend. At lower temperatures, the yield progressively increases with time, whereas at 190 °C it reaches a maximum after 1 h before declining. This behaviour supports our earlier discussion that IPL is an intermediate which can undergo transfer hydrogenation to GVL. Similarly, the effect of temperature on LA conversion was examined using the same catalyst and temperature range. Elevated temperatures also led to improved LA conversion and GVL yield, with almost complete LA conversion (98%) achieved at 190 °C within approximately 4 hours, yielding 78% GVL. Beyond this point, the reactant is spent and GVL yield plateaus. IPL yield followed a similar trend to that observed when EL was used as the reactant; however, more IPL is formed from LA than from EL, particularly at higher temperatures.

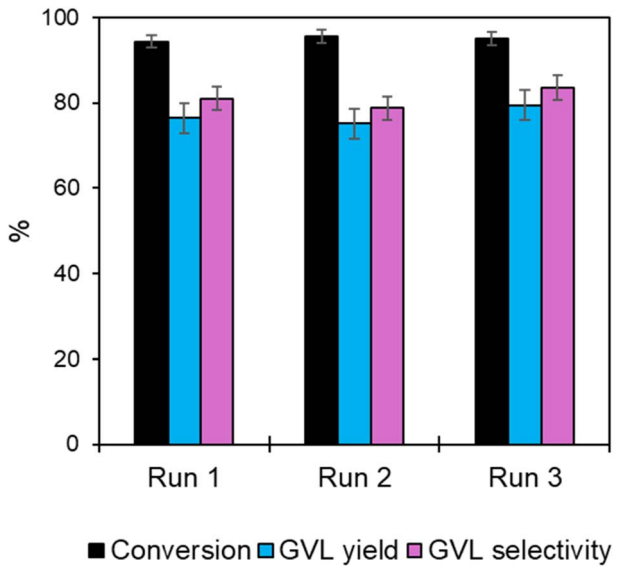

Fig. 12 Recyclability of 6Si/Zr in LA transfer hydrogenation. Reaction conditions: catalyst (100 mg), LA (5 mmol), 2-propanol (250 mmol), internal standard (*n*-dodecane, 0.5 mmol), 5 bar N_2, 170 °C, 6 h.

Recyclability tests were carried out with the 6Si/Zr catalyst across three consecutive reaction cycles. Leaching is a major challenge for solid acids like sulphated zirconia in liquid-phase reactions, particularly in protic solvents such as water and alcohols, and often leads to rapid deactivation.[92,93] In sharp contrast, our catalyst maintained its activity across all three cycles with no detectable loss in performance, as shown by the consistent conversion, yield and selectivity in Fig. 12. Remarkably, this stability was achieved without any calcination between runs, as the catalyst was only washed with fresh 2-propanol and dried. This indicates that the material not only resists leaching but also does not suffer from significant carbonaceous deposits, thereby retaining its performance without high-temperature regeneration. Even when introduced by colloidal deposition, silica interacts strongly with zirconia through the formation of covalent Zr–O–Si linkages that are insoluble in protic solvents. This prevents leaching of the silica and preserves the tailored acidity, leading to a stable catalytic performance. Although longer-term validation is required in continuous mode, the present results demonstrate a clear benefit of this material as it resists immediate leaching and shows excellent stability under the investigated conditions.

As summarised in Table S1, our 6 wt% silica-doped zirconia catalyst (6Si/Zr) demonstrates superior productivity compared with the majority of reported systems for the catalytic transfer hydrogenation of LA to GVL using 2-propanol as hydrogen donor. Noble metal catalysts such as Pd/C, Pt/C and Ru/C, although achieving high conversions, show modest productivities ($\leq$8.2 $mmol_{GVL}\ g_{cat}^{-1}\ h^{-1}$), considering the high catalyst to reactant ratio (172 wt%). Similarly, non-noble systems such as Ni/ZrO_2 and Cu/AC give good GVL yields (88–90%) but remain limited in productivity (<2 $mmol_{GVL}\ g_{cat}^{-1}\ h^{-1}$). In contrast, 6Si/Zr consistently achieves high conversions (82–98%) with good GVL yields (64–80%) and reaches a productivity of 18 $mmol_{GVL}\ g_{cat}^{-1}\ h^{-1}$ at 190 °C. Although higher productivities have been reported for Zr@PS-FA and Ni_3P–$CePO_4$,[26,94] the synthesis of these materials is considerably more complex, making large-scale application less straightforward. The simplicity and effectiveness of Si-doping therefore offer a more practical route to developing efficient and scalable zirconia-based catalysts.

4. Conclusions

This study investigated the CTH of LA and its esters to GVL over silica-doped zirconia catalysts. Varying the silica content significantly altered the physicochemical properties of the material, including acidity, surface area, and crystallinity. Incorporation of moderate silica loading inhibited the sintering of ZrO_2 particles during calcination, promoting the formation of smaller particles and stabilising the tetragonal phase. It also enhanced surface area and the total number of acid sites, however, at 10 wt% Si, these benefits were partially diminished and the material became amorphous. XPS and NEXAFS analyses further confirmed silicon enrichment at the surface and the formation of Si–O–Zr linkages, consistent with the presence of a silica overlayer and its role in modifying the electronic and catalytic environment. The Brønsted-to-Lewis acid site ratio

increased progressively with silica content, influencing the catalytic performance. EL conversion to GVL was favoured over Lewis acid-rich catalysts, whereas LA conversion showed a stronger dependence on Brønsted acidity. IPL, a key intermediate, especially in LA reactions, was also convertible to GVL, albeit less efficiently. Optimal GVL yields were achieved with catalysts possessing a balanced acidity profile. For EL, a Brønsted/Lewis ratio of 0.6 (3 wt% Si) was ideal, whereas LA required a slightly higher ratio of 0.7 (6 wt% Si). Under optimised conditions, a GVL yield of 69% and a productivity of 5.9 $mmol_{GVL}\ g_{cat}^{-1}\ h^{-1}$ from LA was obtained at 170 °C after 6 h. Increasing the temperature to 190 °C led to full LA conversion and 80% GVL yield and a productivity of 18 $mmol_{GVL}\ g_{cat}^{-1}\ h^{-1}$. In addition, the optimal 6Si/Zr catalyst maintained its performance across three consecutive cycles without calcination, confirming resistance to leaching under liquid-phase conditions. Considering the simple and scalable synthesis, low-cost composition, and stability, the silica-doped zirconia catalysts developed here exhibit promising attributes for future scale-up.

Author contributions

Memoona Khalid: validation, formal analysis, investigation, data curation, writing – original draft, visualization, Mark A. Isaacs: validation, formal analysis, investigation, writing – original draft, visualization, Stylianos D. Stefanidis, Stamatia Karakoulia, Nicole Hondow: formal analysis, investigation, writing – review & editing, Dave Scapens, Marta Granollers Mesa: methodology, writing – review & editing, supervision, Amin Osatiashtiani: conceptualization, methodology, resources, writing – review & editing, supervision, funding acquisition.

Conflicts of interest

The authors declare the following potential competing interest: Luxfer MEL Technologies provided financial support for this research. Dave Scapens is an employee of Luxfer MEL Technologies. The other authors declare no competing interests.

Acknowledgements

We thank Luxfer MEL Technologies for their financial support. This work was also supported by UKRI and the Engineering and Physical Sciences Research Council Doctoral Training Partnership (grant number EP/T518128/1). X-ray photoelectron (XPS) data was acquired at the EPSRC National Facility for XPS ("HarwellXPS", EP/Y023587/1, EP/Y023609/1, EP/Y023536/1, EP/Y023552/1 and EP/Y023544/1). NEXAFS work was carried out with the support of Diamond Light Source, instrument B07 (proposal SI40403). Amin Osatiashtiani acknowledges funding from the Royal Society Research Grant RGS\R1\231234.

References

1 L. Cullen, F. Meng, R. Lupton and J. M. Cullen, *Nat. Chem. Eng.*, 2024, **1**, 311–322.
2 Oxford Economics, Report for ICCA.
3 G. Hutchings, *Catalysing Change: Defossilising the Chemical Industry*, The Royal Society, 2024.
4 K. Wilson and A. F. Lee, *Philos. Trans. R. Soc. A Math. Phys. Eng. Sci*, 2016, **374**, 20150081.
5 D. B. Sulis, N. Lavoine, H. Sederoff, X. Jiang, B. M. Marques, K. Lan, C. Cofre-Vega, R. Barrangou and J. P. Wang, *Nat. Commun.*, 2025, **16**, 1244.
6 F. Kerkel, M. Markiewicz, S. Stolte, E. Müller and W. Kunz, *Green Chem.*, 2021, **23**, 2962–2976.
7 W. Fang and H. Sixta, *ChemSusChem*, 2015, **8**, 73–76.
8 R. Trevorah, G. Harding and M. Z. Othman, *Bioresour. Technol. Rep.*, 2020, **11**, 100497.
9 J. Cheng, X. Liu, C. Huang, Y. Zhan, C. Huang, T. Chen, X. Meng, C. G. Yoo, G. Fang and A. J. Ragauskas, *Green Chem.*, 2023, **25**, 6270–6281.
10 X. Wu, S. Xie, D. Vangestel, H. Zhao and B. Sels, *Angew. Chem., Int. Ed.*, 2024, **63**, e202409826.
11 Á. Bereczky, K. Lukács, M. Farkas and S. Dóbé, *Nat. Resour.*, 2014, **5**, 177–191.
12 I. T. Horváth, H. Mehdi, V. Fábos, L. Boda and L. T. Mika, *Green Chem.*, 2008, **10**, 238–242.
13 D. M. Alonso, S. G. Wettstein and J. A. Dumesic, *Green Chem.*, 2013, **15**, 584–595.
14 K. G. Martínez Figueredo, F. A. Martínez, D. J. Segobia and N. M. Bertero, *ChemPlusChem*, 2023, **88**, e202300381.
15 S. Raoufmoghaddam, M. T. M. Rood, F. K. W. Buijze, E. Drent and E. Bouwman, *ChemSusChem*, 2014, **7**, 1984–1990.
16 GF Biochemical starts commercial levulinic acid production, *Biofuels International Magazine*, https://biofuels-news.com/news/gf-biochemical-starts-commercial-levulinic-acid-production/, accessed June 26, 2025.
17 A. Osatiashtiani, A. F. Lee and K. Wilson, *J. Chem. Technol. Biotechnol.*, 2017, **92**, 1125–1135.
18 M. Khalid, M. Granollers Mesa, D. Scapens and A. Osatiashtiani, *ACS Sustainable Chem. Eng.*, 2024, **12**, 16494–16517.
19 A. V. Elbakari, S. V. Vostrikov, R. Siewert, K. Müller and S. P. Verevkin, *Int. J. Hydrogen Energy*, 2024, **84**, 848–862.
20 Y. Kuwahara, W. Kaburagi, Y. Osada, T. Fujitani and H. Yamashita, *Catal. Today*, 2017, **281**, 418–428.
21 T. Tabanelli, E. Paone, P. Blair Vásquez, R. Pietropaolo, F. Cavani and F. Mauriello, *ACS Sustain. Chem. Eng.*, 2019, **7**, 9937–9947.
22 R. Bacchiocchi, A. Ventimiglia, A. Canciani, G. Peroni, T. Tabanelli, S. Albonetti, N. Dimitratos, I. Rivalta, S. Zainal, L. Forster, C. D'Agostino and F. Cavani, *J. Catal.*, 2023, **428**, 115177.
23 H. Chen, Q. Xu, H. Li, J. Liu, X. Liu, G. Huang and D. Yin, *Catal. Lett.*, 2021, **151**, 538–547.
24 X. Cao, H. Dong, H. Chen, Q. Xu and D. Yin, *IOP Conf. Ser. Mater. Sci. Eng.*, 2020, **729**, 12109.
25 X. Liu and Z. Li, *Sustain. Energy Fuels*, 2021, **5**, 3312–3320.
26 Z. Yu, F. Meng, Y. Wang, Z. Sun, Y. Liu, C. Shi, W. Wang and A. Wang, *Ind. Eng. Chem. Res.*, 2020, **59**, 7416–7425.

27 W. Gong, C. Chen, R. Fan, H. Zhang, G. Wang and H. Zhao, *Fuel*, 2018, **231**, 165–171.
28 X. Cao, J. Wei, H. Liu, X. Lv, X. Tang, X. Zeng, Y. Sun, T. Lei, S. Liu and L. Lin, *J. Chem. Technol. Biotechnol.*, 2019, **94**, 167–177.
29 M. T. Jayakumari and C. Kanakkampalayam Krishnan, *Appl. Catal., A*, 2023, **663**, 119318.
30 M. Cabanillas, A. Franco, N. Lázaro, A. M. Balu, R. Luque and A. Pineda, *Mol. Catal.*, 2019, **477**, 110522.
31 C. López-Aguado, M. Paniagua, J. A. Melero, J. Iglesias, P. Juárez, M. López Granados and G. Morales, *Catalysts*, 2020, **10**, 678.
32 M. Paniagua, G. Morales, J. A. Melero, J. Iglesias, C. López-Aguado, N. Vidal, R. Mariscal, M. López-Granados and I. Martínez-Salazar, *Catal. Today*, 2021, **367**, 228–238.
33 A. Osatiashtiani, S. A. Orr, L. J. Durndell, I. C. García, A. Merenda, A. F. Lee and K. Wilson, *Catal. Sci. Technol.*, 2022, **12**, 5611–5619.
34 L. Soumoy, A. Maertens, A. Morena, L. Fusaro, M. Armandi, S. Fiorilli, D. P. Debecker and C. Aprile, *Mater. Today Chem.*, 2024, **40**, 102189.
35 F. Li, L. J. France, Z. Cai, Y. Li, S. Liu, H. Lou, J. Long and X. Li, *Appl. Catal. B Environ.*, 2017, **214**, 67–77.
36 A. Merenda, S. A. Orr, Y. Liu, B. Hernández Garcia, A. Osatiashtiani, G. Morales, M. Paniagua, J. A. Melero, A. F. Lee and K. Wilson, *ChemCatChem*, 2023, **15**, e202201224.
37 A. Osatiashtiani, A. F. Lee, D. R. Brown, J. A. Melero, G. Morales and K. Wilson, *Catal. Sci. Technol.*, 2014, **4**, 333–342.
38 A. I. M. Rabee, G. A. H. Mekhemer, A. Osatiashtiani, M. A. Isaacs, A. F. Lee, K. Wilson and M. I. Zaki, *Catalysts*, 2017, **7**, 204.
39 J. A. Vannucci, N. N. Nichio and F. Pompeo, *Catal. Today*, 2021, **372**, 238–245.
40 M. Delarmelina, G. Deshmukh, A. Goguet, C. R. A. Catlow and H. Manyar, *J. Phys. Chem. C*, 2021, **125**, 27578–27595.
41 A. Aboulayt, T. Onfroy, A. Travert, G. Clet and F. Maugé, *Appl. Catal., A*, 2017, **530**, 193–202.
42 A. J. Saviola, K. Wijaya, A. Syoufian, W. D. Saputri, D. A. Saputra, I. T. A. Aziz and W.-C. Oh, *Case Stud. Chem. Environ. Eng.*, 2024, **9**, 100653.
43 M. L. Testa and V. La Parola, *Catalysts*, 2021, **11**, 1143.
44 G. D. Yadav and A. D. Murkute, *J. Catal.*, 2004, **224**, 218–223.
45 Y. Zhang, W.-T. Wong and K.-F. Yung, *Bioresour. Technol.*, 2013, **147**, 59–64.
46 A. Amoozadeh, S. Rahmani, M. Bitaraf, F. B. Abadi and E. Tabrizian, *New J. Chem.*, 2016, **40**, 770–780.
47 W. Ciptonugroho, M. G. Al-Shaal, J. B. Mensah and R. Palkovits, *J. Catal.*, 2016, **340**, 17–29.
48 W. Ciptonugroho, J. B. Mensah, G. Al-Shaal and R. Palkovits, *Chem. Pap.*, 2023, **77**, 3769–3778.
49 C. H. Giang, A. Osatiashtiani, V. C. dos Santos, A. F. Lee, D. R. Wilson, K. W. Waldron and K. Wilson, *Catalysts*, 2014, **4**, 414–426.
50 J. He, H. Li, Y.-M. Lu, Y.-X. Liu, Z.-B. Wu, D.-Y. Hu and S. Yang, *Appl. Catal., A*, 2016, **510**, 11–19.
51 T. Yang, H. Li, J. He, Y. Liu, W. Zhao, Z. Wang, X. Ji and S. Yang, *ACS Omega*, 2017, **2**, 1047–1054.
52 D. Zhao, T. Su, D. Rodríguez-Padrón, H. Lü, C. Len, R. Luque and Z. Yang, *Mater. Today Chem.*, 2022, **24**, 100745.
53 Z. Wang, Y. Jiang, M. Hunger, A. Baiker and J. Huang, *ChemCatChem*, 2014, **6**, 2970–2975.
54 N. Scotti, S. Borsacchi, S. Monti, A. Zimina, C. Evangelisti, M. Geppi, P. Dambruoso, G. Barcaro, F. Bossola, V. Dal Santo and N. Ravasio, *J. Alloys Compd.*, 2024, **992**, 174545.
55 R. Zhao, S. Kasipandi, C.-H. Shin and J. W. Bae, *ACS Catal.*, 2023, **13**, 12711–12722.
56 E. De La Rosa-Cruz, L. A. Díaz-Torres, P. Salas, V. M. Castaño and J. M. Hernández, *J. Phys. D: Appl. Phys.*, 2001, **34**, L83.
57 D. N. Argyriou and C. J. Howard, *J Appl Cryst*, 1995, **28**, 206–208.
58 R. C. Garvie, *J. Phys. Chem.*, 1978, **82**, 218–224.
59 K. Sato, H. Abe and S. Ohara, *J. Am. Chem. Soc.*, 2010, **132**, 2538–2539.
60 N. Wu, X. Ji, R. An, C. Liu and X. Lu, *AIChE J.*, 2017, **63**, 4595–4603.
61 N. S. Hassan, A. A. Jalil, F. F. A. Aziz, M. A. H. Aziz, I. Hussain and M. W. Ali, *Mater. Lett.*, 2021, **291**, 129582.
62 H. Y. Jeong, J. H. Lee and K. F. Hayes, *Geochim. Cosmochim. Acta*, 2008, **72**, 493–505.
63 J. B. Miller and E. I. Ko, *J. Catal.*, 1996, **159**, 58–68.
64 Z. Zhan and H. C. Zeng, *J. Non-Cryst. Solids*, 1999, **243**, 26–38.
65 J. Chandradass, K. S. Han and D. sik Bae, *J. Mater. Process. Technol.*, 2008, **206**, 315–321.
66 S. Pyen, E. Hong, M. Shin, Y. W. Suh and C. H. Shin, *Mol. Catal.*, 2018, **448**, 71–77.
67 J. R. Sohn and H. J. Jang, *J. Mol. Catal.*, 1991, **64**, 349–360.
68 S. Jeong, G. L. Sudibya, J.-K. Jeon, Y.-M. Kim, C. M. Swamidoss and S. Kim, *Catalysts*, 2019, **9**, 901.
69 R. Barthos, F. Lónyi, J. Engelhardt and J. Valyon, *Top. Catal.*, 2000, **10**, 79–87.
70 M. Tamura, K.-I. Shimizu and A. Satsuma, *Appl. Catal., A*, 2012, 135–145.
71 S. Pyen, E. Hong, M. Shin, Y. W. Suh and C. H. Shin, *Mol. Catal.*, 2018, **448**, 71–77.
72 A. T. Y. Wolek, K. E. Hicks and J. M. Notestein, *J. Catal.*, 2023, **426**, 113–125.
73 D. J. Morgan, *Surf. Interface Anal.*, 2025, **57**, 28–35.
74 G. Greczynski and L. Hultman, *Nat. Rev. Mater.*, 2025, **10**, 62–78.
75 C. M. A. Parlett, L. J. Durndell, A. Machado, G. Cibin, D. W. Bruce, N. S. Hondow, K. Wilson and A. F. Lee, *Catal. Today*, 2014, **229**, 46–55.
76 C. D. Easton and D. J. Morgan, *J. Vac. Sci. Technol. A*, 2025, **43**, 053205.
77 M. A. Isaacs, C. Drivas, A. Graf, S. Kroon, S. Kumar, J. Liu, A. Torres-Lopez, C. Price, E. Garland, I. Lezcano-Gonzalez, C. M. A. Parlett, V. C. dos Santos-Durndell and L. J. Durndell, *Adv. Funct. Mater.*, 2025, e02818.
78 P. Bhatt, M. Isaacs, Y. Liu and R. G. Palgrave, *Appl. Surf. Sci.*, 2024, **672**, 160808.
79 J. M. Montero, D. R. Brown, P. L. Gai, A. F. Lee and K. Wilson, *Chem.–Eng. J.*, 2010, **161**, 332–339.

80 S. Tougaard, *Surf. Interface Anal.*, 1988, **11**, 453–472.
81 R. Franke, S. Bender, H. Jüngermann, M. Kroschel and M. Jansen, *J. Electron Spectrosc. Relat. Phenom.*, 1999, **101–103**, 641–645.
82 J. Wang, S. Jaenicke and G.-K. Chuah, *RSC Adv.*, 2014, **4**, 13481–13489.
83 Y. Zhu, G. K. Chuah and S. Jaenicke, *J. Catal.*, 2006, **241**, 25–33.
84 Y. Zhu, G. Chuah and S. Jaenicke, *J. Catal.*, 2004, **227**, 1–10.
85 E. Baráth, *Catalysts*, 2018, **8**, 671.
86 A. Corma, M. E. Domine and S. Valencia, *J. Catal.*, 2003, **215**, 294–304.
87 A. Comas-Vives, G. Ujaque and A. Lledós, *J. Mol. Struct.*, 2009, **903**, 123–132.
88 D. Klomp, T. Maschmeyer, U. Hanefeld and J. A. Peters, *Chem.–Eur. J.*, 2004, **10**, 2088–2093.
89 J. S. M. Samec, J.-E. Bäckvall, P. G. Andersson and P. Brandt, *Chem. Soc. Rev.*, 2006, **35**, 237–248.
90 M. Chia and J. A. Dumesic, *Chem. Commun.*, 2011, **47**, 39.
91 H. Neuvonen, K. Neuvonen, A. Koch, E. Kleinpeter and P. Pasanen, *J. Org. Chem.*, 2002, **67**, 6995–7003.
92 Y. Shao, Y. Li, K. Sun, Z. Zhang, H. Tian, G. Gao, Q. Li, Q. Liu, Q. Liu and X. Hu, *Energy Technol.*, 2020, **8**, 1900951.
93 Y. Kuwahara, W. Kaburagi, K. Nemoto and T. Fujitani, *Appl. Catal., A*, 2014, **476**, 186–196.
94 Y. Liu, F. Chen, J. Zhang, L. He and L. Peng, *Fuel*, 2022, **315**, 123150.